

Revisiting tea-leaf paradox with a deformable spoon

Benjamin Apffel* and Romain Fleury

*Institute of Electrical and Micro Engineering, Laboratory of Wave Engineering,
Ecole Polytechnique Fédérale de Lausanne (EPFL), Station 11, 1015 Lausanne, Switzerland*

(Dated: July 8, 2024)

The tea-leaf paradox refers to the migration of tea leaves toward the center of a tea cup when the water is put in rotation by a spoon. Although much attention has been given to liquid and particle transport generated by a spoon, the back-action of the generated flow on a deformable spoon has not been considered. In this work, we therefore propose to revisit the tea-leaf paradox with a deformable stirrer consisting of a floating ball attached to a soft string. The later is set in rotation and the ball trajectory results from the balance between string tension and the back action of the surrounding flow, leading to surprising effects. At low rotation speeds, we show that the circular trajectory of the ball shrinks when we stir faster, which contradicts common intuition based on inertia. For higher rotation rates, the ball is either suddenly attracted toward the center, or is repulsed away from it, depending on the string length. A model explaining these observations is proposed, and validated using experimental measurements of the generated flow. Interestingly, the system exhibits strong hysteretic behavior, leading to a modified version of the tea-leaf paradox in which the spoon itself can be trapped at the center in the flow generated by its past motion.

In its simplest version, the tea leaf paradox arises when mixing a liquid with a spoon performing circular trajectories (Fig. 1a). The paradox arises when one notices that particles placed at the bottom tend to aggregate at the center of the cup rather than on the outside, as expected from centrifugal force. The transport arises due to three-dimensional flow generated along the vertical direction by the edges of the container [1]. Such flows imposed by boundary conditions are of prime interest from geophysics to physical chemistry and microfluidics, for example to understand the preferential concentration of sediments concentration near a river bank's meanders [2–6], dissolution mediated by rotating paddles [7], for controlling the aggregation of nanoparticles [8] or blood-plasma separation [9, 10].

The back action of the flow generated by rotating free-to-move objects has also been investigated. For instance, magnetic disks placed in rotation at a liquid interface were shown to interact and self-assemble under the generated flow's action [11–13], and interact with their environment [14, 15]. More generally, the interplay between deformable bodies and flow generation is at the heart of propulsion mechanisms for living organisms [16–19] or robots [20–22], an idealized case of such situation being the flow disturbance generated by a flexible plate [23–25].

Inspired by these works, we propose here to revisit the tea leaf paradox with a deformable spoon, and to focus on the motion of the later rather than on the flow (Fig. 1a). As an experimental model, we study the motion of a ball attached to one end of an inextensible string, the other end being attached to a rotating arm as in Fig. 1b-c. Imposing a circular trajectory results in the emergence of several unexpected phenomena that we describe in this work. First, the radius of the stirrer's circular trajectory surprisingly decreases when the rotation rate

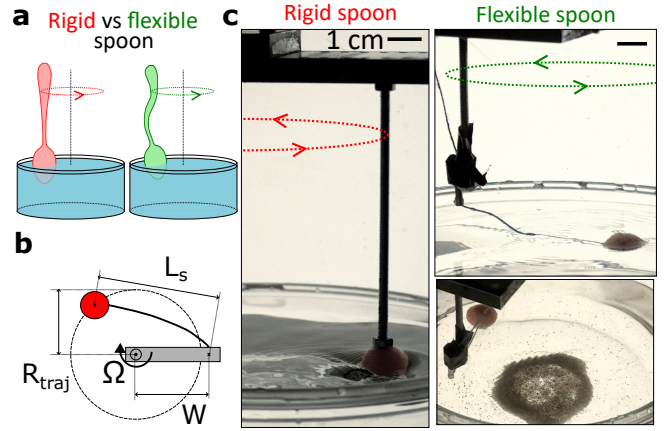


FIG. 1. (a) Sketch of a rigid and a deformable spoon mixing a liquid. (b) Definition of geometrical parameters for the flexible stirrer consisting of a plastic ball of radius 7 mm pulled by an inextensible string attached to a rotation arm. (c) Experimental idealization of a rigid spoon (left) using a metallic stem, and its deformable counterpart made by replacing the stem by a wool strand (top right). The flow induced by the deformable stirrer transports particles (pepper grains) placed at the bottom near the center, showing that the tea leaf paradox still occurs in this case (bottom right).

increases. This holds until a critical rotation speed is reached, for which a strong bifurcation occurs and the ball is either suddenly attracted toward the center, or repelled outwards, depending on the string length. A model explaining these observations is developed, and we then show in particular that the lift force generated by the ball's motion must be taken into account to satisfactory explain the result. A quantitative criteria for the appearance of the collapsed regime is derived, and we show that strong hysteresis is observed once the stirrer is trapped.

All experiments (except illustrations of Fig. 1) are conducted in a rectangular tank of $55 \times 55 \text{ cm}^2$ and filled

* benjamin.apffel@epfl.ch

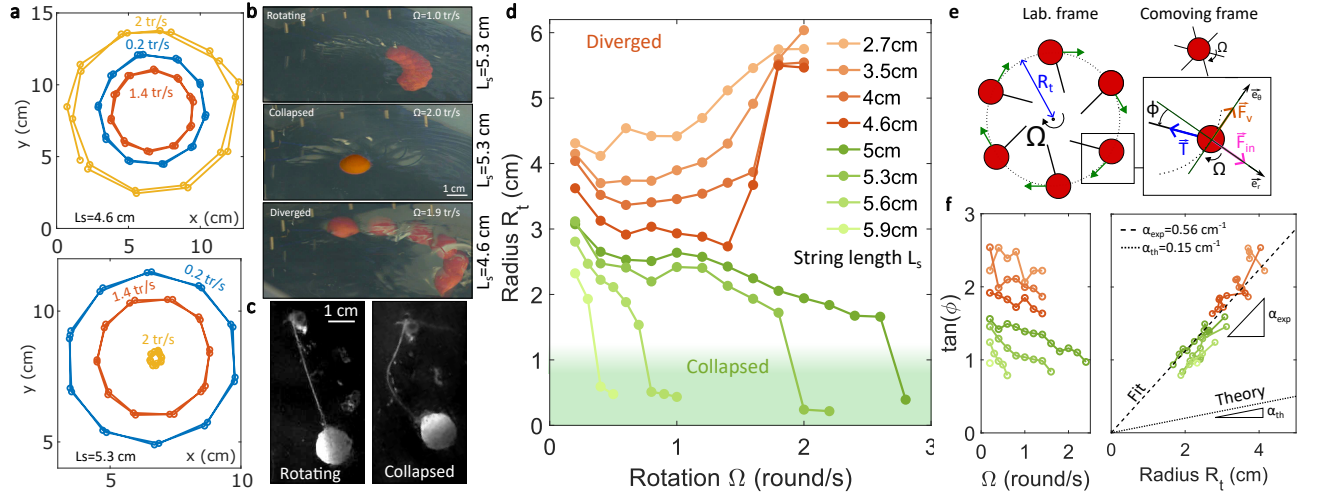


FIG. 2. (a) Example of experimentally measured trajectories for different rotation speed $\Omega = 0.2, 1.4, 2$ round/s and two different string length $L_s = 4.6$ cm (top) and $L_s = 5.3$ cm (bottom). (b) Experimental kinogrammes showing a circular trajectory (top), a collapsed state (middle) and a diverging state (bottom). (c) Picture from below showing the loss of tension in the string when a collapsed state is reached. (d) Radius of the trajectory as a function of the rotation speed for different string length L_s . For the shortest strings ($L_s \leq 4.6$ cm), the ball reaches a diverging state while longest strings ($L_s \geq 5$ cm) lead to collapsing states. (e) Motion of the ball in the laboratory or comoving frame and definition of the forces and angles. (f) Experimental measurement of $\tan(\phi)$ (with ϕ the rope angle $(-\vec{e}_r, \vec{T})$) for different string length as a function of rotation speed Ω (left) and trajectory radius R_t (right). All data collapse in a single line of slope $a_{exp} = 0.56 \text{ cm}^{-1}$ (dashed line) while theory predicts $a_{th} = 0.14 \text{ cm}^{-1}$ (dot line).

with tap water with depth 6.5 cm, preventing the ball to get close from any edge. A model rigid spoon has been built using a 3D-printed plastic ball of radius $R_s = 7$ mm and mass $m = 1.2$ g at the end of a metallic stem (Fig 1c). A stepper motor is used to set it up in rotation with rate $\Omega \sim 1$ round/s, and the rotation arm length is fixed to $W = 4.4$ cm. This model spoon is made flexible by replacing the stem by a strand of wool of length L_s and diameter ≤ 0.2 mm as sketched in Fig. 1b. Such strand is, in our regimes, non-extensible, of negligible mass compared to the ball and free of static or plastic deformation after being constrained. As we aim to study here the ball's motion at the fluid interface, the final version of the setup includes a small tube to guide the strand close from the water surface as in Fig. 1c. This allows to confine the deformable system in the horizontal plane while avoiding the introduction of constraints on the string. When the rotation is turned on, a short transient regime of duration less than 10s is observed during which the ball converges toward a circular trajectory or radius R_t . On a minute scale, articles placed at the bottom converge toward the center of the tank (see Fig. 1c and supplementary movies), showing that three dimensional flows and associated transport ('tea-leaf' paradox) still occur with our model deformable spoon. In what follows, we will focus on the surprising properties of the stirrer's motion.

A camera (Basler) placed below the tank records 10 images per revolution of the rotation arm (see Fig. 2c for a typical image). The ball's position is retrieved on each image using a convolution algorithm detailed in the

Supplementary Informations (SI). Examples of measured trajectories are shown in Fig. 2a for two string length $L_s = 4.6$ cm, $L_s = 5.3$ cm and different rotation speeds $\Omega = 0.2, 1.4$ and 2 round/s. The trajectories are circular in all cases but their radius R_t strongly depends on the rotation speed and the string length. Several remarkable features can be observed. First, when the rotation speed increases from 0.2 round/s to 1.4 round/s, the radius of the trajectory decreases. This is opposite from what one occurs when the ball hangs in the air, for which the increasing centrifugal force pushes the ball more on the outside. Second, for the case $L_s = 5.3$ cm, the ball reaches a trajectory with zero radius for $\Omega = 2$ round/s, and the string goes from straight to curved shape (Fig. 2c). In this case, the ball simply spins at the center in what we will call a 'collapsed' or 'self-trapped' behavior. For a slightly shorter string $L_s = 4.6$ cm, the same rotation speed $\Omega = 2$ round/s gives rise to opposite behavior as the radius of the trajectory brutally increases, in what we call a 'diverging' behavior. Kinogrammes obtained by stacking images from the side are shown in Fig. 2b and display the three regimes discussed above (see also supplementary movies). Experiment snapshots in Fig. 2c show that the string is straight in non-collapsed cases, but gains some curvature in the collapsed state.

More systematic experiments allow to plot the trajectory's radius as a function of rotation rate for different string length varying from 2.7 cm to 5.9 cm. The results are shown in Fig. 2d. Aside from the smallest values of string length $L_s = 2.7$ cm, two regimes can be identified. Starting at low rotation rate, increasing the later leads to

diminishing the radius trajectory. This holds until a critical rotation rate, for which the system exhibits strong bifurcation and the radius brutally changes. Depending on the string length, the ball is either suddenly expelled to the outward or attracted in the inward of the circular trajectory, corresponding to diverging and collapsing behavior discussed above. The first case occurs for $L_s \leq 4.6$ cm, while the second case is observed for $L_s \geq 5$ cm.

We now propose to perform an analysis of the forces acting on the ball in the comoving frame. We will restrain ourselves to the case where the string is tensed and the immersed volume constant. From experimental observations, this corresponds to the cases where the trajectory radius diminishes with Ω without being collapsed (see SI for details on data selection). For now, we will consider the inertial force \vec{F}_{in} , the viscous force \vec{F}_v and the string tension \vec{T} sketched in Fig. 2e. We assume that the ball performs a circular motion of radius R_t with rotation speed Ω . The inertial force due to the acceleration writes $\vec{F}_{in} = 3/2 m R_t \Omega^2 \vec{e}_r$ where the $3/2$ factor accounts for the added mass of fluid that needs to be pushed by the sphere. As Reynolds number Re typically ranges from 500 to 5000 in our experiments, we take a quadratic law for the viscous force $\vec{F}_v = 1/2 \rho C_D S_{im} (R_t \Omega)^2 \vec{e}_\theta$ with $C_D \approx 0.4$ is the dimensionless drag parameter [26] and $S_{im} \approx 0.8\pi R^2$ is the immersed cross-sectional surface of the object in the direction of the motion.

As the ball is steady in the comoving frame, one gets $\vec{T} = -\vec{F}_{in} - \vec{F}_v$. In particular, the angle $\phi = (-\vec{e}_r, \vec{T})$ (see Fig. 3a) can be expressed as

$$\tan(\phi) = \frac{F_v}{F_{in}} = \alpha_{th} R_t \quad (1)$$

where $\alpha_{th} \approx 0.24 C_D / R_s$. Experimental measurements of $\tan(\phi_d)$ as a function of Ω are shown in Fig. 2f. All measurements collapse on a single curve $\tan(\phi) = \alpha_{exp} R_t$ as shown in 2f, confirming the scaling law in Eq. 1. However, the measured experimental value $\alpha_{exp} = 0.56 \text{ cm}^{-1}$ is much larger than the predicted value $\alpha_{th} = 0.14 \text{ cm}^{-1}$.

Such discrepancy can be solved by considering the additional lift force produced by the fluid. The later is generated by the complete solid rotation of the sphere during its revolution, shown in Fig. 2e, combined with non-zero relative velocity of the ball with respect to the fluid [27, 28]. A quantitative characterization of the resulting surface flow is performed using particle image velocimetry (PIV) measurement with PIVLab [29, 30]. The liquid surface was seeded with small particles (pepper grains) while water was made opaque using a bit of powder milk to ensure good contrast. A camera placed above the tank recorded 150 frames/s during a full revolution of the ball, ensuring small displacement of the ball and the particles between two images. A stack of 15 consecutive images is shown in Fig. 4a. The same stack in the co-moving frame shows the streamline's bending by the ball. From this picture, one can expect a lift force directed toward the inward of the trajectory. Its magnitude can be estimated starting from the lift force on a cylinder of height

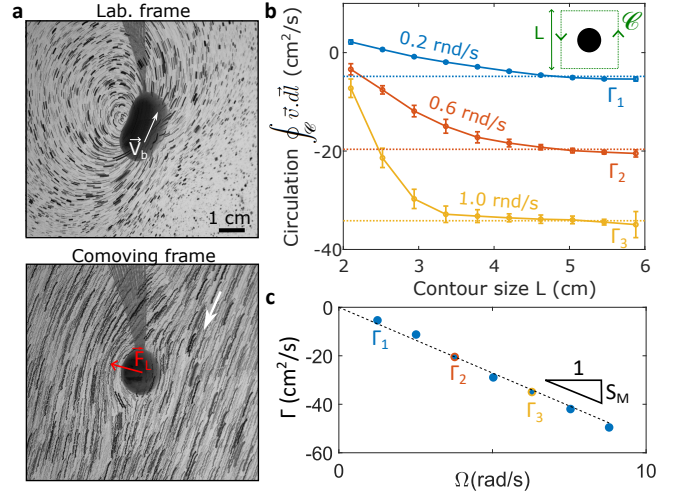


FIG. 3. (a) Stack of 15 consecutive images taken at 150 frame/s showing the motion of particles at the water surface in the laboratory (top) and comoving (bottom) frame. Direction of lift force \vec{F}_L and fluid motion is also indicated. (b) Experimental measurement of velocity field's circulation using PIV for different contour sizes and three different rotation rate of the ball. Error bar show the standard deviation of the measurement over 40 consecutive images. (c) Circulation as a function of rotation speed and linear fit $\Gamma = S_M \Omega$ with $S_M = -5.4 \text{ cm}^2$.

D in a two dimensional flow [27, 31]

$$\vec{F}_L = \rho D R_t \Omega \Gamma \vec{e}_r \quad (2)$$

where $\Gamma = \oint \vec{v} \cdot d\vec{l}$ is the circulation taken around the object far from the boundary layer. The circulation at the water surface can be measured experimentally from PIV measurement. The contour we chose is a square of side L centered on the ball as shown in Fig. 3b. The circulation Γ for different contour size L is shown in the same figure for three rotation rates $\Omega = 0.2, 0.6, 1.0$ rad/s. The error bars are computed from the standard deviation on the measurement over 40 consecutive frames, showing low dispersion of measurement along time. As the size of the contour increases, the circulation increases and eventually reaches a plateau for the largest contours, which is the circulation value Γ introduced in Eq. (2) [27]. The later is shown as a function of the rotation rate in Fig. 3c and shows excellent agreement with a linear fit $\Gamma = S_M \Omega$ with $S_M = -5.4 \text{ cm}^2$. The lift force can therefore be expressed as $\vec{F}_M = -M R_t \Omega^2 \vec{e}_r$ with $M = \rho D S_M$ homogeneous to a mass and D a distance let as a free parameter for now. The lift force scales exactly as the inertial force but with an effective negative mass. One must therefore modify Eq. 1 as

$$\tan(\phi) = \frac{a_{th}}{1 - 2M/3m} R_t \quad (3)$$

The linear relation $\Gamma \propto \Omega$ ensures that both equations (1) and (3) have similar dependency with R_t but with an

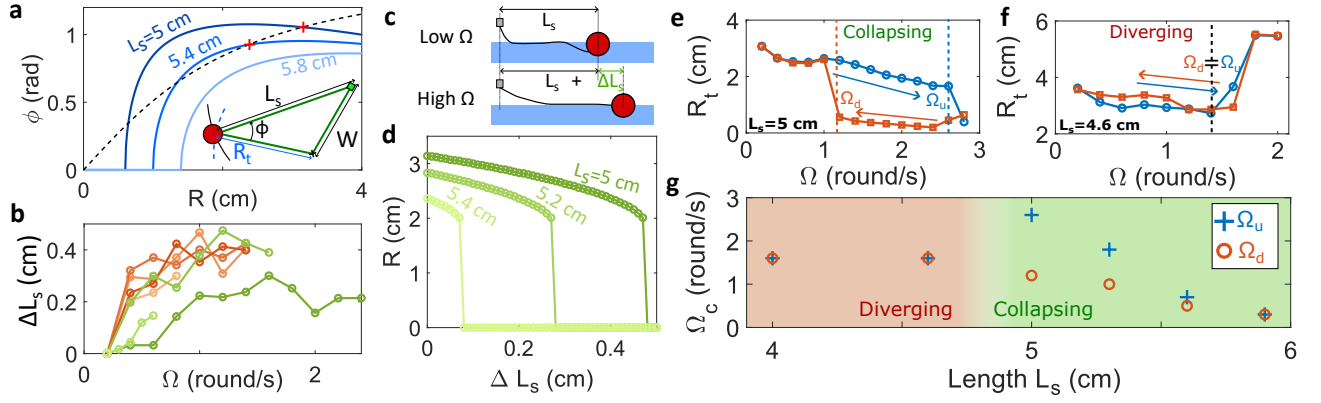


FIG. 4. (a) Angle ϕ as a function of the trajectory radius R_t for different string length L_s according to Eq. (4) (color lines) and to force equilibrium of Eq. (1) (dashed line). Either zero or two equilibrium angles fulfill both constraints depending on L_s , and only the largest one is stable in the later case (red crosses). (b) Increasing string elongation ΔL_s measured experimentally as a function of Ω of different string length. (c) Elongation of the string in the horizontal plane due to increasing tension with Ω . (d) Radius of the equilibrium trajectories when the string is elongated from L_s to $L_s + \Delta L_s$. (e) Radius of the trajectory for the diverging (left, $L_s = 4.6$ cm) and collapsing (right, $L_s = 5.0$ cm) when the rotation speed is progressively increased (blue circles) or decreased (red squares) (f) Critical rotation speeds Ω_u and Ω_d as a function of string length L_s .

increasing prefactor in the second case, which is perfectly consistent with our results. Using the found value α_{exp} in Eq. (3) fixes the only free parameter of our model $D = 0.3$ cm. For a purely two-dimensional flow, D should exactly be the penetration length of the sphere in water, which is 1.0 cm. The mismatch between the two can be attributed to the spherical shape of our object as well as to possible three-dimensional flows generation, in line with the particle's motion discussed in Fig. 1b.

So far, we have shown that our experimental measurement were consistent with the force analysis expressed in Eq. (1). Nevertheless, this is not enough to predict the trajectories radius R_t shown in Fig. 2d. The later can be fully determined if one assumes that the string is straight. In this case, the triangle formed by the ball, the hooking point and the rotation center (Fig. 4a) imposes an extra relationship between the geometrical parameters that reads

$$\phi = \arccos\left(\frac{L_s^2 + R_t^2 - W^2}{2L_s R_t}\right) \quad (4)$$

A plot of this geometrical constrain is shown in Fig. 4a for $L_s = 5, 5.2$ and 5.4 cm (plain colored lines), while force equilibrium from Eq. (1) is represented by the black dashed line. For smallest string length, two solutions (ϕ, R_t) are found while no solution exists when L_s is too large. Among the two solutions, one can show that only the largest one materialized by red crosses in Fig. 4a is stable (see SI). This finally fully determines the radius trajectory for a given string length.

The last step comes by noticing that the string length in the interface plane (also denoted L_s) increases with the rotation rate. This is shown by experimental measurement of the string elongation $\Delta L_s = L_s(\Omega) - L_s(\Omega_0)$ in Fig. 4b, which is by definition zero for $\Omega_0 = 0.2$ round/s. We observed experimentally that the string's edges tends

to become more horizontal when Ω increases, as sketched in Fig. 4c (see also pictures in SI). The tension increase, which scales as $T \propto \Omega^2$, leads to three-dimensional reorganization of the inextensible string and to the apparent flexibility in the horizontal plane. It is this varying string length in the horizontal plane that should be taken into account for the geometrical constrain (4). The resulting equilibrium radius R_t therefore depends on the elongation ΔL_s and is plotted in Fig. 4d for three initial string length and various elongations. The radius R_t progressively decreases when the later increases, which is consistent with our experimental observations. The collapse of the system can also be interpreted as the loss of solutions discussed in Fig. 4a when the string becomes too long. In this case, the ball's equilibrium and the string tension cannot be guaranteed simultaneously, which leads to a shape change of the rope. The later occurs for smaller values of elongation when the initial string length is larger. Last, the predicted value for the radius before collapse is approximately 2 cm and independent of L_s . All those features are remarkably consistent with our experimental results of Fig. 2d.

A last aspect of the ball's motion is the stability of the collapsed state. Starting from a collapsed state obtained for $L_s = 5$ cm and $\Omega_u = 2.6$ round/s (blue circles in Fig. 4e), we progressively decrease the rotation speed. Interestingly, the ball remains trapped until Ω goes below $\Omega_d = 1.2$ round/s (red squares), for which circular trajectories appear again. Such hysteresis was observed in all collapsing configurations, but not in the diverging case as shown in Fig. 4f. We plot in Fig. 4g the critical rotation speeds Ω_u and Ω_d for various string length L_s . Their difference decreases with L_s , showing that the hysteresis is stronger near the transition between diverging and collapsing behavior for a reason that is still to be understood. The hysteresis is due to the existence of a

memory in the system, which can be qualitatively interpreted in two ways. First, the tension lost in the string needs to be recovered to expel the ball from the flow's center. Second, the surrounding flow exhibits circular symmetry that needs to be broken to recover circular trajectories. Both features require a strong perturbation to be broken, leading to a robust hysteresis.

We have discussed in this work the circular motion of a ball pulled by a string and show the prime importance of the string's deformation and flow's action to explain the variety of observed trajectories. This opens several interesting avenues for the future. Our results first strongly suggests to perform the same experiments with several

objects to introduce pairwise interactions mediated by the flow as done in other systems [11]. It would also be interesting to replace water with a non-newtonian fluid, which were for instance shown to modify swimmers efficiency [32]. Last, replacing the inextensible rope by a flexible one could also lead to new physical features that are still to explore.

ACKNOWLEDGMENTS

The authors acknowledge J.B. Gorce for fruitful discussions and M. Mallejac for his help with Blender.

-
- [1] James Thomson and William Thomson, "V. On the origin of windings of rivers in alluvial plains, with remarks on the flow of water round bends in pipes," *Proceedings of the Royal Society of London* **25**, 5–8 (1997), publisher: Royal Society.
 - [2] A. Einstein, "Die Ursache der Mäanderbildung der Fluviale und des sogenannten Baerschen Gesetzes," *Naturwissenschaften* **14**, 223–224 (1926).
 - [3] J.F. Friedkin, *A Laboratory Study of the Meandering of Alluvial Rivers* (United States Waterways experiment station, 1945) google-Books-ID: d4HuAAAAMAAJ.
 - [4] Kent Bowker, "Albert Einstein and Meandering Rivers," *Earth Sciences History* **7**, 45 (2007).
 - [5] L B Leopold and M. G. Wolman, "River Meanders," *GSA Bulletin* **71**, 769–793 (1960).
 - [6] R G. Jackson, II, "Velocitybed-formtexture patterns of meander bends in the lower Wabash River of Illinois and Indiana," *GSA Bulletin* **86**, 1511–1522 (1975).
 - [7] Leonard G. McCarthy, Carolin Kosiol, Anne Marie Healy, Geoff Bradley, James C. Sexton, and Owen I. Corrigan, "Simulating the hydrodynamic conditions in the united states pharmacopeia paddle dissolution apparatus," *AAPS PharmSciTech* **4**, 22 (2003).
 - [8] Zehui Zhang, Bin Zhou, Mingtao Jia, Chengbin Wu, Tingting Niu, Chen Feng, Hongqiang Wang, Yanfeng Liu, Jialu Lu, Zhihua Zhang, Jun Shen, and Ai Du, "Einstein's tea leaf paradox induced localized aggregation of nanoparticles and their conversion to gold aerogels," *Science Advances* **9**, eadi9108 (2023), publisher: American Association for the Advancement of Science.
 - [9] Leslie Y. Yeo, James R. Friend, and Dian R. Arifin, "Electric tempest in a teacup: The tea leaf analogy to microfluidic blood plasma separation," *Applied Physics Letters* **89**, 103516 (2006).
 - [10] Dian R. Arifin, Leslie Y. Yeo, and James R. Friend, "Microfluidic blood plasma separation via bulk electrohydrodynamic flows," *Biomicrofluidics* **1**, 014103 (2006).
 - [11] Bartosz A. Grzybowski, Howard A. Stone, and George M. Whitesides, "Dynamic self-assembly of magnetized, millimetre-sized objects rotating at a liquidair interface," *Nature* **405**, 1033–1036 (2000), publisher: Nature Publishing Group.
 - [12] Bartosz A. Grzybowski, Xingyu Jiang, Howard A. Stone, and George M. Whitesides, "Dynamic, self-assembled aggregates of magnetized, millimeter-sized objects rotating at the liquid-air interface: Macroscopic, two-dimensional classical artificial atoms and molecules," *Physical Review E* **64**, 011603 (2001), publisher: American Physical Society.
 - [13] Bartosz A. Grzybowski, Howard A. Stone, and George M. Whitesides, "Dynamics of self assembly of magnetized disks rotating at the liquidair interface," *Proceedings of the National Academy of Sciences* **99**, 4147–4151 (2002), publisher: Proceedings of the National Academy of Sciences.
 - [14] Jean-Baptiste Gorce, Hua Xia, Nicolas Francois, Horst Punzmann, Gregory Falkovich, and Michael Shats, "Confinement of surface spinners in liquid metamaterials," *Proceedings of the National Academy of Sciences* **116**, 25424–25429 (2019), publisher: Proceedings of the National Academy of Sciences.
 - [15] Jean-Baptiste Gorce, Konstantin Y. Bliokh, Hua Xia, Nicolas Francois, Horst Punzmann, and Michael Shats, "Rolling spinners on the water surface," *Science Advances* **7**, eabd4632 (2021), publisher: American Association for the Advancement of Science.
 - [16] Mattia Gazzola, Mdric Argentina, and L. Mahadevan, "Scaling macroscopic aquatic locomotion," *Nature Physics* **10**, 758–761 (2014), publisher: Nature Publishing Group.
 - [17] Geoffrey Ingram Taylor, "Analysis of the swimming of microscopic organisms," *Proceedings of the Royal Society of London. Series A. Mathematical and Physical Sciences* **209**, 447–461 (1997), publisher: Royal Society.
 - [18] Theodore Yaotsu Wu, "Fish Swimming and Bird/Insect Flight," *Annual Review of Fluid Mechanics* **43**, 25–58 (2011), publisher: Annual Reviews.
 - [19] Intesaaf Ashraf, Hana Bradshaw, Thanh-Tung Ha, Jos Halloy, Ramiro Godoy-Diana, and Benjamin Thiria, "Simple phalanx pattern leads to energy saving in cohesive fish schooling," *Proceedings of the National Academy of Sciences* **114**, 9599–9604 (2017), publisher: Proceedings of the National Academy of Sciences.
 - [20] Sara Oliveira Santos, Nils Tack, Yunxing Su, Francisco Cuenca-Jimenez, Oscar Morales-Lopez, P. Antonio Gomez-Valdez, and Monica M. Wilhelmus, "Pleobot: a modular robotic solution for metachronal swimming," *Scientific Reports* **13**, 9574 (2023), publisher: Nature Publishing Group.
 - [21] Christopher J. Esposito, James L. Tangorra, Brooke E.

- Flammang, and George V. Lauder, “A robotic fish caudal fin: effects of stiffness and motor program on locomotor performance,” *The Journal of Experimental Biology* **215**, 56–67 (2012).
- [22] J. Zhu, C. White, D. K. Wainwright, V. Di Santo, G. V. Lauder, and H. Bart-Smith, “Tuna robotics: A high-frequency experimental platform exploring the performance space of swimming fishes,” *Science Robotics* **4**, eaax4615 (2019), publisher: American Association for the Advancement of Science.
- [23] T. Yao-Tsu Wu, “Swimming of a waving plate,” *Journal of Fluid Mechanics* **10**, 321–344 (1961).
- [24] Silas Alben, “Collective locomotion of two-dimensional lattices of flapping plates. Part 1. Numerical method, single-plate case and lattice input power,” *Journal of Fluid Mechanics* **915**, A20 (2021).
- [25] Jonathan Toomey and Jeff D. Eldredge, “Numerical and experimental study of the fluid dynamics of a flapping wing with low order flexibility,” *Physics of Fluids* **20**, 073603 (2008).
- [26] Christophe Clanet, “Sports Ballistics,” *Annual Review of Fluid Mechanics* **47**, 455–478 (2015), publisher: Annual Reviews.
- [27] Gregory Falkovich, *Fluid Mechanics*, p. 56, 2nd ed. (Cambridge University Press, Cambridge, 2018).
- [28] S. I. Rubinow and Joseph B. Keller, “The transverse force on a spinning sphere moving in a viscous fluid,” *Journal of Fluid Mechanics* **11**, 447–459 (1961).
- [29] William Thielicke and Eize J. Stamhuis, “PIVlab Towards User-friendly, Affordable and Accurate Digital Particle Image Velocimetry in MATLAB,” *Journal of Open Research Software* **2** (2014), 10.5334/jors.bl.
- [30] William Thielicke and Ren Sonntag, “Particle Image Velocimetry for MATLAB: Accuracy and enhanced algorithms in PIVlab,” *Journal of Open Research Software* **9** (2021), 10.5334/jors.334.
- [31] Guillaume Dupeux, Anne Le Goff, David Qur, and Christophe Clanet, “The spinning ball spiral,” *New Journal of Physics* **12**, 093004 (2010).
- [32] Julian Espinosa-Garcia, Eric Lauga, and Roberto Zenit, “Fluid elasticity increases the locomotion of flexible swimmers,” *Physics of Fluids* **25**, 031701 (2013).

Supplementary Materials - Revisiting tea-leaf paradox with a deformable spoon

Benjamin Apffel* and Romain Fleury

*Institute of Electrical and Micro Engineering, Laboratory of Wave Engineering,
Ecole Polytechnique Fédérale de Lausanne (EPFL), Station 11, 1015 Lausanne, Switzerland*

(Dated: July 8, 2024)

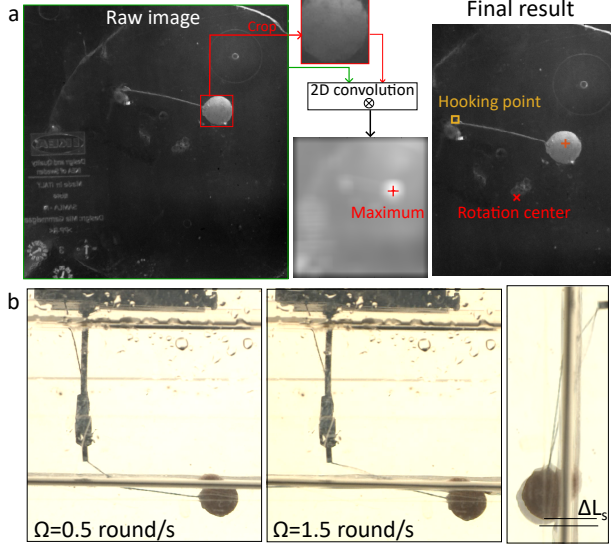


FIG. 1. (a) Example of image analysis: a raw image (left) is 2D-convoluted with the image of the ball (middle-top). The maximum of the resulting image (middle-bottom) has maximum value at the center of the ball. This allows to recover the ball's position (right). The position of the hooking point (yellow square) and of the rotating center (red X) is also shown. (b) Example of shape change of the string as the rotation speed goes from 0.5 round/s (left) to 1.5 round/s (middle) with $L_s = 4.4$ cm. A superposition of the two images (right) shows the length increase ΔL_s in the horizontal plane.

EXPERIMENTAL METHODS

Trajectory and angle measurement

In order to recover the ball's trajectory, a camera is placed below the tank and records 10 images/revolution of the ball. A raw image is shown in Fig. 1. The ball appears brighter than the background, but contrast analysis has shown some failure. We therefore performed 2D convolution of the raw image with the image of the ball, and the resulting image has clear maximum at the ball's location. Performing similar analysis on each image gives trajectories $((x(t), y(t)))$ as shown in Fig.1 of the main text. The rotation center (X cross in Fig. 1) is obtained by computing the mean value of x and y over several revolutions. In order to measure the angle ϕ , one also needs to get the position of the hooking point. The later is simply spot on a single image. We have checked that the particular image chosen does not affect significantly

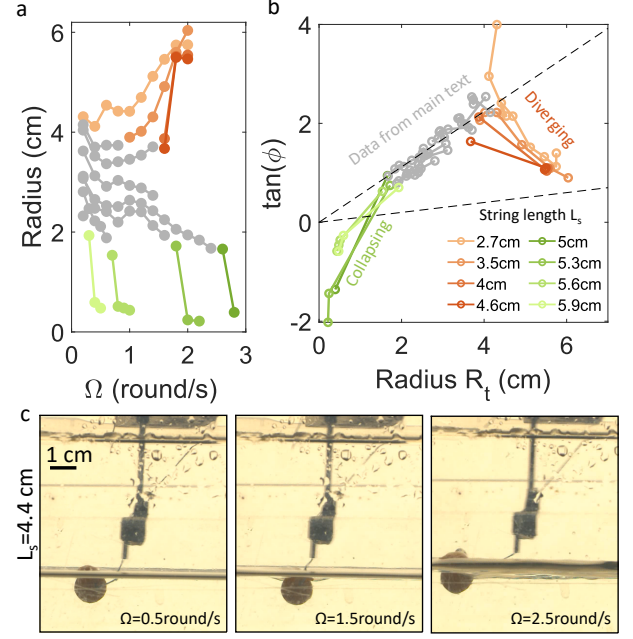


FIG. 2. (a-b) (Colors) Excluded data from angle analysis in the main text, for which only the gray points were kept. (c) Side view of the ball for $L_s = 4.4$ cm showing the up lift experienced by the ball for largest values of Ω .

L_s (cm)	2.7	3.5	4	4.6	5	5.3	5.6	5.9
Ω_{lim} (round/s)	0	1	1.6	1.6	2.8	1.8	0.7	0.3

TABLE I. Maximum rotation value considered for each string length for data selection in angle measurement

the measurement result.

String elongation in the horizontal plane

We have discussed in the main text the reorganization of the string which leads to an increase of its length in the horizontal plane. Such effect is shown in Fig. 1b and the superposition of two images from the side for $\Omega = 0.5$ round/s and 1.5 round/s shows the string elongation ΔL_s of approximately 2 mm between the two. This is consistent and complementary with the results presented in the main text.

Data selection for angle measurement

As discussed in the main text, some data selection has been performed in the main text between radius measurement of Fig. 1d and angle measurement of Fig. 1f. First, all data corresponding to collapsed states have been discarded since the rope is not shaped as a straight line in those cases (green points in Fig. 2). The proposed model was therefore irrelevant for those data, hence their exclusion.

We also decided to exclude all data associated with an increase of the radius, which corresponds to red-colored points in Fig. S2 associated with $\Omega \geq \Omega_{lim}(L_s)$ with the value Ω_{lim} summarized in table 1. In particular, all data from $L_s = 2.7$ cm were excluded. We indeed observed that when the radius increases, the immersed volume of the ball was diminishing. Such phenomena can be seen on Fig. 2c, where the immersed volume of the ball decreases significantly between $\Omega = 1.5$ round/s (non-diverging) to $\Omega = 2.5$ round/s (diverging). As the proposed model assumes constant immersed volume, it is not surprising that the corresponding points do not match with the prediction (Fig. 2b). Correcting the model to take this phenomena is beyond the scope of this work but we strongly believe that this varying immersed volume could lead to other interesting regimes. In particular, our data suggest that the up-lift experienced by the ball appears for larger Ω and more brutally as the string length increases. The origin of this lift is not clear to us at this stage but is an interesting perspective of this work.

STABILITY OF EQUILIBRIUM POSITIONS

We have shown in the main text that the equilibrium angle ϕ must fulfill both the force equilibrium condition which reads

$$\tan(\phi) = \alpha_{th} R_t \quad (1)$$

as well as the geometric condition deduced from the triangle formed by the ball, the hooking point and the rotation center

$$\cos(\phi) = \frac{L_s^2 + R_t^2 - W^2}{2L_s R_t} \quad (2)$$

A graphical analysis shows that this equation admits two solutions when L_s is small enough and zero if it is too large. The later case was interpreted as the collapsing behavior. When two solutions exists, only the largest one is stable. This can be shown by writing the equation of motion of the ball in the laboratory frame assuming constant rotation speed $\dot{\theta} = \Omega$ (which can be positive or negative) but not constant radius r

$$\frac{3}{2}m(\ddot{r} - r\Omega^2)\vec{e}_r + 3m\dot{r}\Omega\vec{e}_\theta = \vec{T} + \vec{F}_v \quad (3)$$

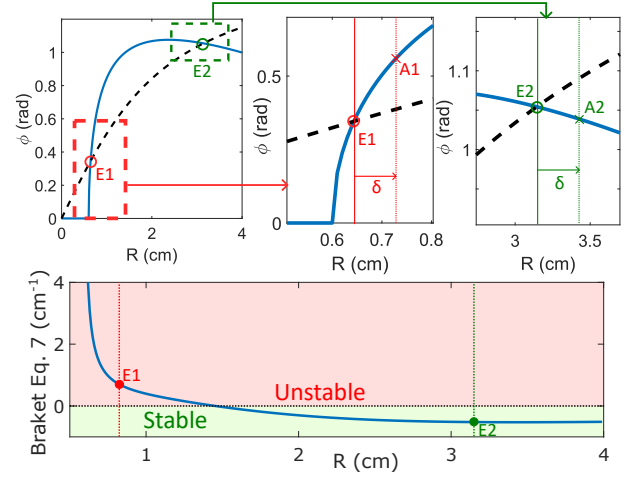


FIG. 3. Stability analysis. Upper panels: angle ϕ determined from Eq. (1) (black dashed line) and geometrical constrain (2) (blue plain line). The two equilibrium positions are denoted E1 and E2, and insets show small perturbations A1 and A2 for stability analysis. The later is determined by the lower panel which plots $d \tan \phi / dR - 1/R_t$ from Eq. 7. Positive sign implies unstable equilibrium while negative sign ensures stability.

We will now perform some perturbation around the equilibrium radius R_t and write $r = R_t + \delta$ with $\delta \ll R_t$. For simplicity, we will also assume that return at equilibrium occurs slowly so that $\dot{\delta} \ll R_t \Omega$. From this, we get to first order the viscous force as

$$\vec{F}_v = \frac{-1}{2} \rho C_L S_{im} R_t^2 \Omega |\Omega| \left(1 + \frac{\delta}{R_t}\right) \left(\frac{\dot{\delta}}{R_t \Omega} \vec{e}_r + \left(1 + \frac{\delta}{R_t}\right) \vec{e}_\theta\right) \quad (4)$$

After some calculation, one finds

$$\tan \phi - \tan \phi_{eq} = \frac{\delta}{R_t} - \frac{2 + \tan(\phi_{eq})^2}{\tan(\phi_{eq})} \frac{\dot{\delta}}{R_t \Omega} + \frac{\ddot{\delta}}{R_t \Omega^2} \quad (5)$$

and remembering that $S_{im} \approx 0.8\pi R^2$ and $m \approx 0.8\rho(4/3\pi R^3)$, one has

$$\tan(\phi_{eq}) = \frac{-\rho C_D S_{im} R_t}{2m} \frac{\Omega}{|\Omega|} \approx -\frac{C_D}{4R_s} \frac{\Omega}{|\Omega|} \quad (6)$$

which is consistent with the expression in the main text as $\Omega < 0$ in our convention.

We can now perform a linear stability analysis of the two equilibrium solutions which can be seen on Fig. 3. To plot those graphs, we have taken the case $\Omega < 0$ resulting in $\tan \phi_{eq} > 0$ and so $\phi > 0$. For simplicity, we will neglect the $\ddot{\delta}$ term, which corresponds to assume that $\ddot{\delta} \ll \dot{\delta} \Omega$ consistent with the hypothesis of slow return to equilibrium. E. (5) can now be recast as

$$\frac{\dot{\delta}}{V_0} = \left[\left(\frac{d \tan \phi}{dR} \right)_{\phi_{eq}} - \frac{1}{R_t} \right] \delta \quad (7)$$

with

$$V_0 = R_t |\Omega| \frac{\tan(\phi_{eq})}{(2 + \tan(\phi_{eq}))^2} > 0 \quad (8)$$

We first consider the stability of the largest equilibrium position E2 (right panel of Fig. 3). If one perturbs the equilibrium by pushing a bit the ball on the outside ($\delta > 0$) while keeping the string tensed so that one remains on the plain blue line, one has $\phi < \phi_{eq}$ (point A2 in the plot). Therefore, one has $\frac{d \tan \phi}{dR} < 0$ and the bracket in Eq. (7) is negative, leading to $\dot{\delta} < 0$. The same analysis for $\delta < 0$ leads to $\dot{\delta} > 0$, and this equilibrium position is

therefore stable.

On the other hand, one can consider the smallest equilibrium position E1 (middle panel of Fig. 3) and a perturbation with $\delta > 0$ corresponding to A1. In this case, one has $\frac{d \tan \phi}{dR} > 0$ so that the sign in the bracket of Eq. 7 is undefined. Nevertheless, one can see on Fig. 3 that the derivative $d\phi/dR$ near E1 is very large (~ 3 rad/cm) while $1/R \sim 1.5$ cm⁻¹. Therefore, the bracket will be positive and one has $\dot{\delta} > 0$, so that the equilibrium position is unstable. This is confirmed by Fig. 3b which plots the bracket of Eq. (7) that changes sign between the two equilibrium points.